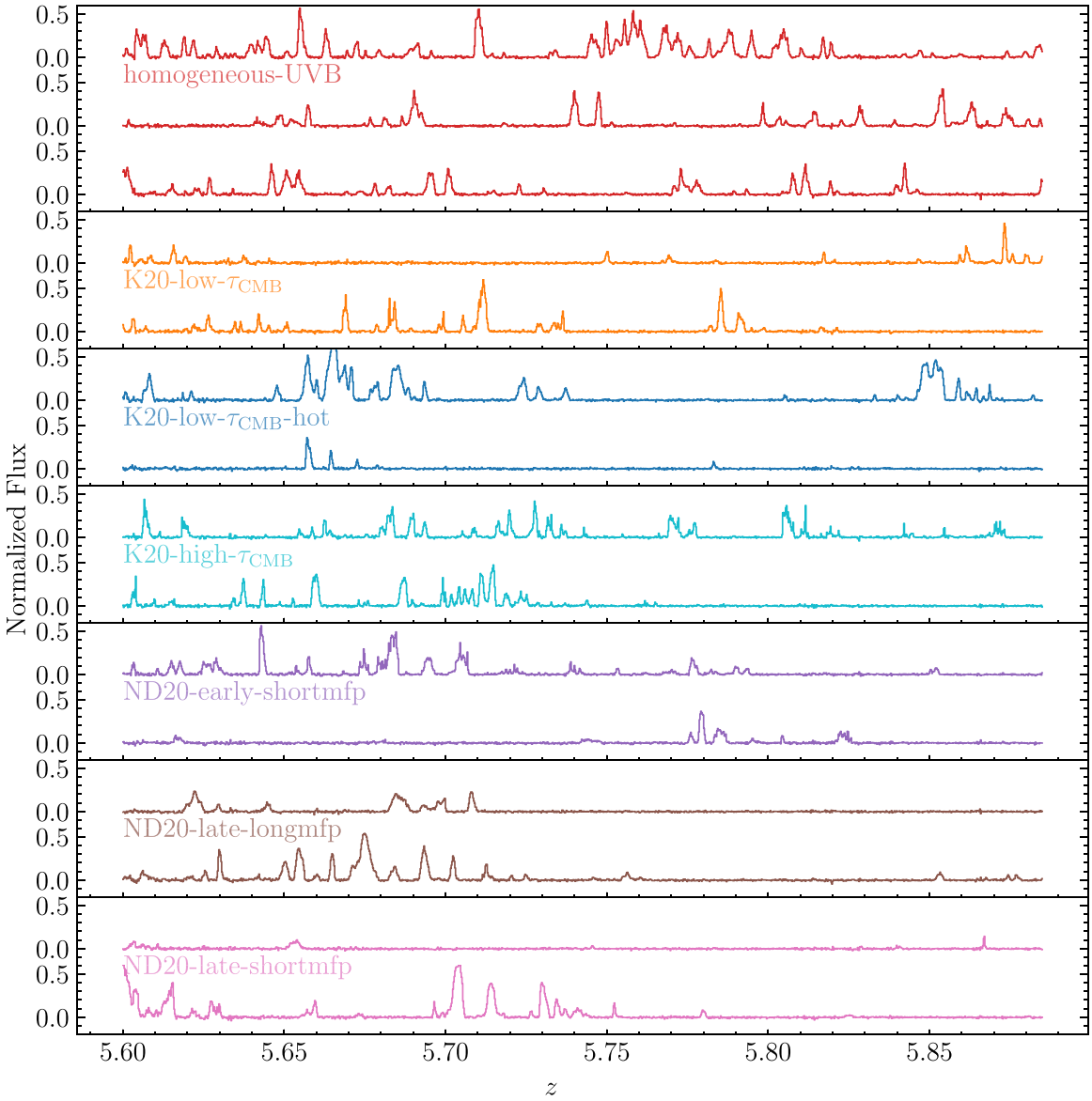

Figure 8. Example mock spectra with binning and S/N chosen to match the Lyα forest of ULAS J0148+0600. We randomly select mock sightlines from each model here. The colored lines represent the flux arrays.

UVB fluctuations also play a significant role in producing the dark gaps in the late reionization models.

5. Discussion

5.1. Model Comparisons

We now compare our results to predictions from the simulations described in Section 4. Figure 11 plots the dark gap length versus central redshift for representative mock samples drawn from the `homogeneous-UVB` model and the `K20-low-`$\tau_{\rm CMB}$ model. Qualitatively, as redshift increases, the `homogeneous-UVB` model predicts a milder increase in long dark gaps than is seen in either the `K20-low-`$\tau_{\rm CMB}$ model or the observations (Figure 3). To quantify the differences, we compute the relevant statistics by drawing mock samples from the simulations that match our observed QSO spectra in redshift and S/N ratio. We then compute the dark gap statistics described in Section 3. We repeat this process 10,000 times for each model and compute the mean, 68% limit, and 95% limit on the expected scatter for the present sample size. Figure 12 compares F_{30} predicted by models to that calculated from data. The jagged edges of the simulation confidence intervals are caused by the combined effects of step changes in the number of sightlines with redshift and the quantization of F_{30} for a finite sample size.

The top left panel shows that the `homogeneous-UVB` model is highly inconsistent with the observations over $5.3 \lesssim z \lesssim 5.9$. At $z \sim 5.8$, the `homogeneous-UVB` model under-predicts F_{30} by a factor of 3. At $z \sim 5.4$ and over $5.5 \lesssim z \lesssim 5.8$, this model is rejected by the data with $> 99.9\%$ confidence.

On the other hand, the `K20-low-`$\tau_{\rm CMB}$ and `K20-low-`$\tau_{\rm CMB}$`-hot` models, wherein reionization ends at $z \simeq 5.3$, produce F_{30} results that are generally consistent with the observations over $5 < z < 6$. One exception is that these models underpredict the small number of long dark gaps observed at $z \sim 5.4$. The `K20-high-`$\tau_{\rm CMB}$ model is consistent with the observations at $z \geqslant 5.75$ but underpredicts F_{30} at lower redshifts.

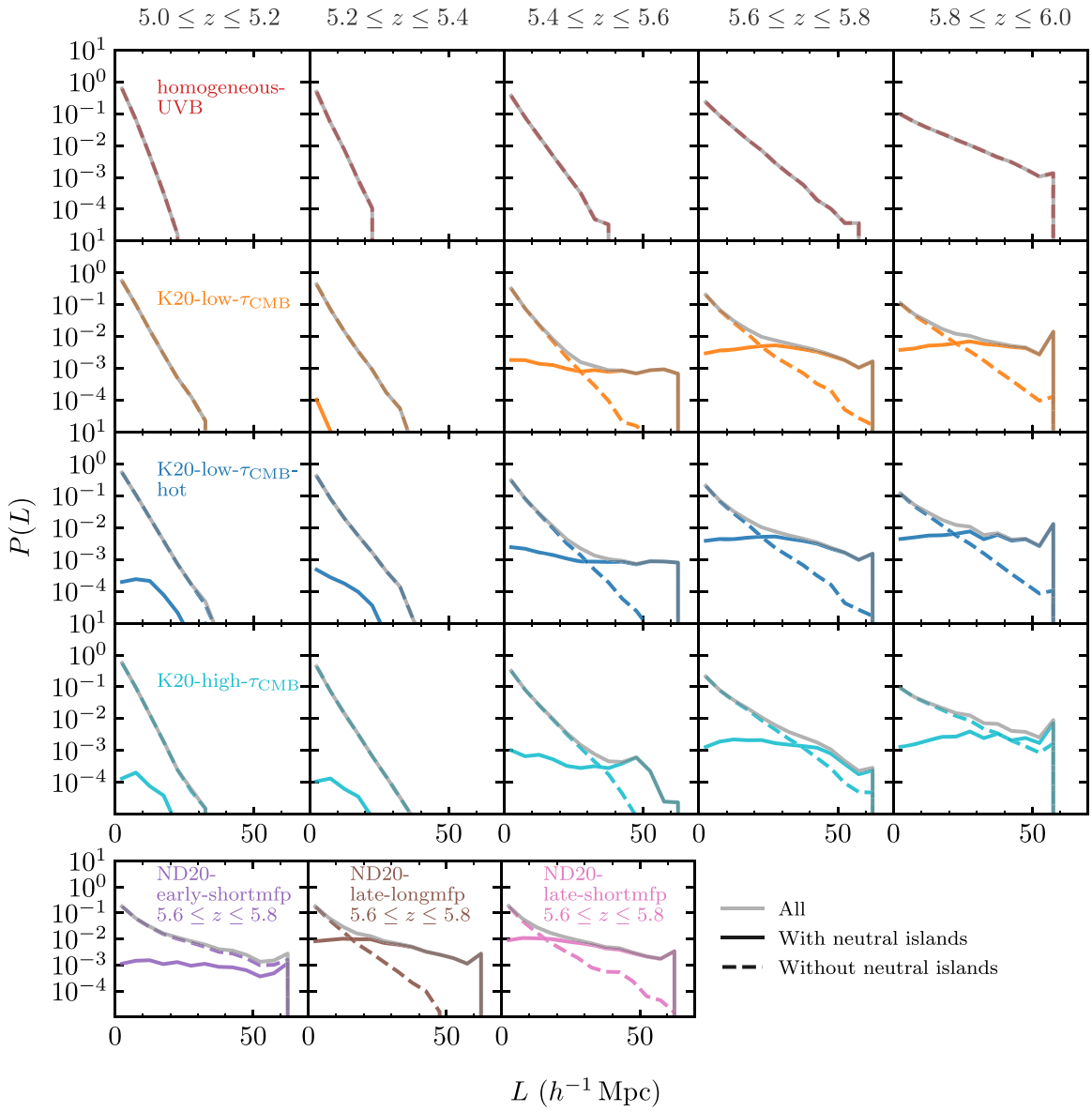

Figure 9. Distribution of dark gaps with and without neutral hydrogen predicted by simulations. A dark gap is considered to contain neutral gas if any pixels inside this gap have a neutral fraction of $x_{\rm HI} > 0.9$. $P(L)$ is calculated with count of dark gaps over $\Delta L = 5h^{-1}$ Mpc bins divided by the total count of dark gaps. The distribution is calculated with dark gaps detected in 10,000 sets of mock spectra (Section 4.4) for each simulation, but with no noise added. We note that the volume neutral fraction information of Nasir & D'Aloisio (2020) models is only available at $z = 5.6$ and 5.8. The plots for `ND20` models are therefore not extended to $z = 6.0$.

This is a natural consequence of the earlier reionization in this model, which leads to a lower neutral hydrogen fraction and smaller UVB fluctuations at these redshifts.

As shown in the right panels, F_{30} values from the Nasir & D'Aloisio (2020) models are consistent with the observations within their 95% limits over the available redshift range. Among the `ND20` models, `ND20-early-shortmfp` gives lower F_{30} values compared to `ND20-late`, but the difference is within the 68% range for the present sample size.

We compare the cumulative distributions of dark gap length in Figure 13, and give the differences between the observation and the model predictions in Figure 14. In order to facilitate a direct comparison between the observations and simulations, we divide the data into redshift bins of $\Delta z = 0.2$. Here, dark gaps extending beyond the boundaries of a redshift bin are truncated at the edge when calculating $P(< L)$ for both the observation and models. Similar to our approach in Section 4.5, we do this to avoid artifacts from the finite length of the mock spectra.

We present numerical convergence tests for the `homogeneous-UVB` model in Appendix A. We find that the results for both F_{30} and $P(< L)$ are relatively insensitive to box size, but that the number of small gaps increases with increasing mass resolution. The impact of mass resolution is more significant for $P(< L)$ at smaller gap lengths than for F_{30}. For $P(< L)$ measured from the `homogeneous-UVB` model, therefore, we display predictions based on a higher-resolution run with 2×2048^3 particles and a box size of $L = 40h^{-1}$ Mpc (hereafter `40_2048`) instead of the fiducial configuration of 2×2048^3 particles and box size of $L = 160h^{-1}$ Mpc (hereafter `160_2048`). Because Keating et al. (2020a) use postprocessed radiative transfer simulations, and Nasir & D'Aloisio (2020) simulations are based on an Eulerian code instead of a SPH code, mass resolution effects

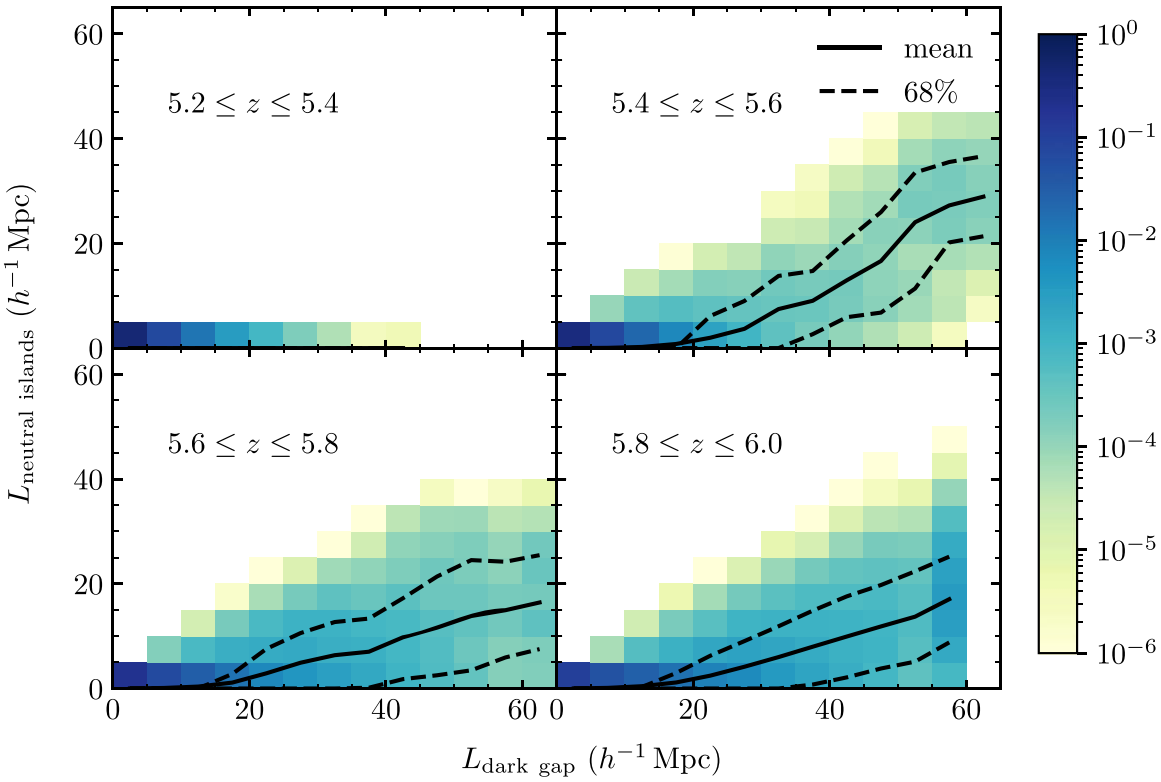

Figure 10. Correlation between neutral islands coverage and dark gap length in the `K20-low-`$\tau_{\rm CMB}$ model based on 10,000 realizations. The histogram is calculated on 5×5 (h^{-1} Mpc)^2 bins with color indicating the normalized probability, and all dark gaps are included regardless of whether they contain neutral gas. Solid and dashed lines show the mean and 68% interval of the neutral islands coverage.

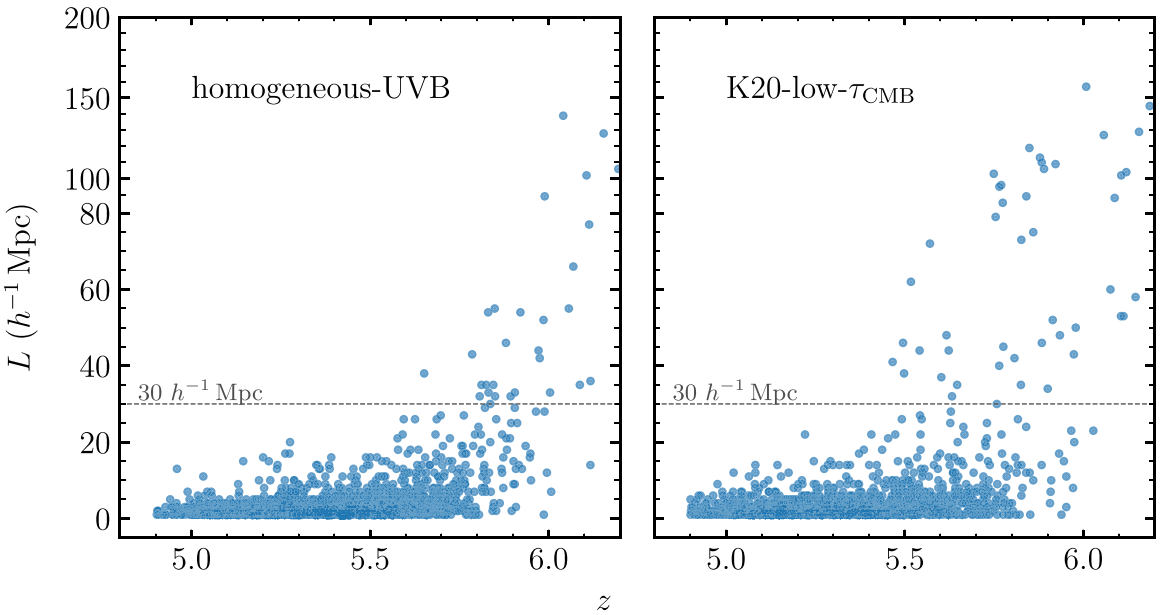

Figure 11. Gap length vs. central redshift for dark gaps detected in mock spectra. For both models, the results shown here are based on one randomly selected set of mock spectra that matches our QSO sample in redshift and S/N ratio.

may be significantly different for these models than for the `homogeneous-UVB` model. We therefore present results as they are, although mass resolution corrections may be needed.

Over $z = 5.6$–6.0, the `homogeneous-UVB` model predicts significantly fewer long gaps than are observed in the data. The discrepancies between the data and the `homogeneous-UVB` model persist down to the $z = 5.2$–5.4 bin.

In contrast, the late reionization models, `K20-low-`$\tau_{\rm CMB}$, `K20-low-`$\tau_{\rm CMB}$`-hot`, and `K20-high-`$\tau_{\rm CMB}$, predict $P(<L)$ values that are generally consistent with the data. Nevertheless, over $z = 5.7$–5.9, we note that these models, especially the `K20-high-`$\tau_{\rm CMB}$ model, systematically yield higher $P(<L)$, i.e., fewer long gaps, than the observed for some L, though the discrepancies are less conspicuous compared to those for the `homogeneous-UVB`. At lower

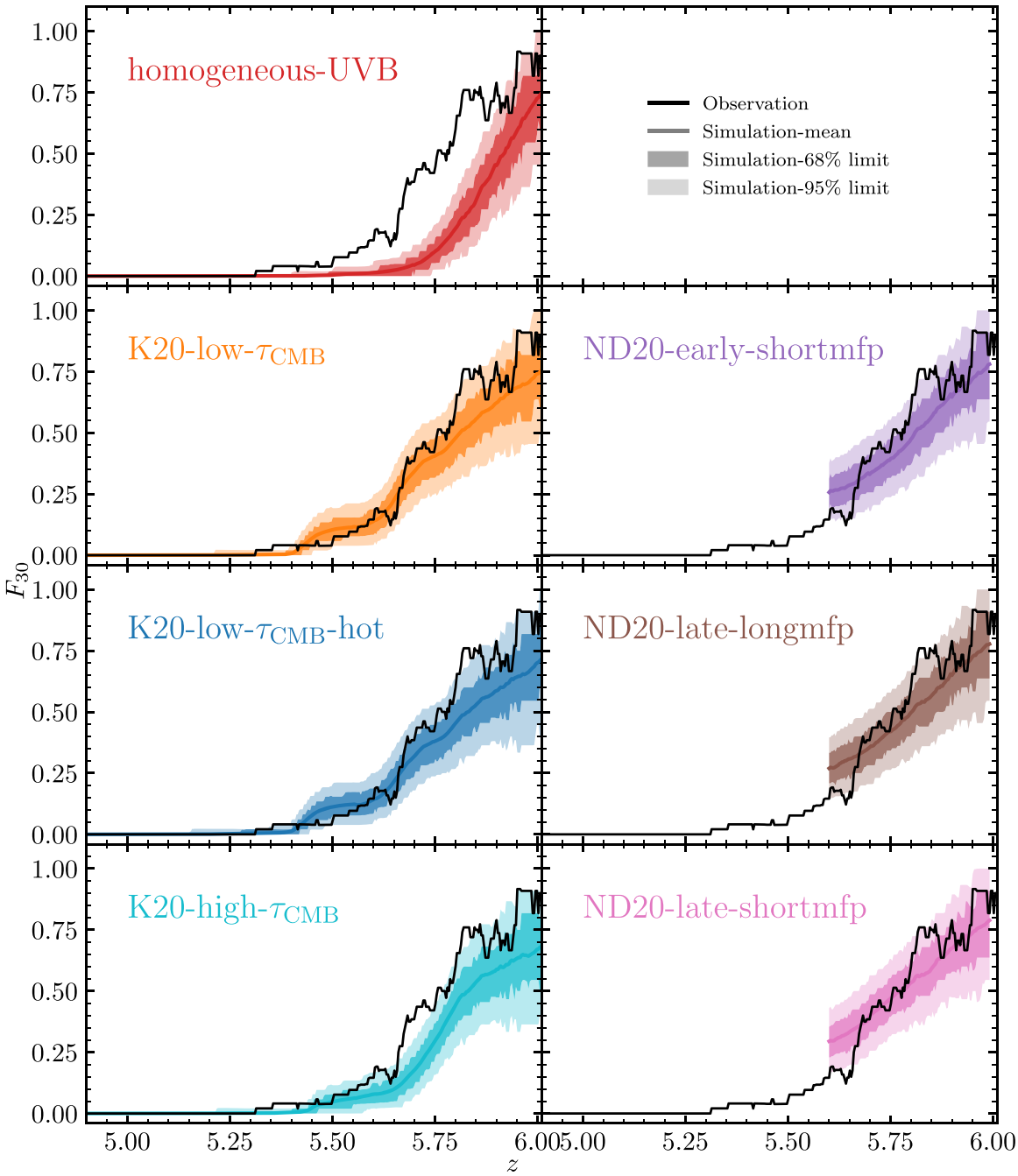

Figure 12. The fraction of sightlines located in dark gaps with $L \geqslant 30h^{-1}$ Mpc as a function of redshift. Both the observations (solid black line) and simulations (colored solid line and shaded regions) include gaps that are truncated at the red end of the Lyα forest. Note that we discard dark gaps that are entirely in the 7 pMpc proximity zone and/or in the buffer zone that covers $30h^{-1}$ Mpc blueward the proximity zone cut. Dark and light shaded regions show the 68% and 95% intervals, respectively, spanned by the models.

redshifts, there are minor differences between the `K20` models and the observation. The `ND20-early-shortmfp` and `ND20-late` models are generally consistent with the observation in the redshift range ($5.6 \leqslant z \leqslant 6.0$) currently probed by the simulations.

5.2. Implications for Reionization

Combining the results for F_{30} and $P(< L)$, it is evident that a fully ionized IGM with a homogeneous UV background is disfavored by the observations down to $z \sim 5.3$. This result is consistent with the large-scale inhomogeneities in IGM Lyα opacity seen in recent $\tau_{\rm eff}$ measurements (Becker et al. 2015; Bosman et al. 2018; Eilers et al. 2018; Yang et al. 2020b; Bosman et al. 2021a). Our results also agree with the early indication from Gnedin et al. (2017) that models, wherein reionization ended well before $z = 6$, struggled to produce enough long dark gaps.

The late reionization models from Keating et al. (2020a) and Nasir & D'Aloisio (2020) are generally consistent with dark gap statistics in the Lyα forest. In these models, the residual neutral islands at $z < 6$ coupled with UVB fluctuations can naturally explain the appearance of long dark gaps in the Lyα forest. Among these models, the data tend to prefer those with

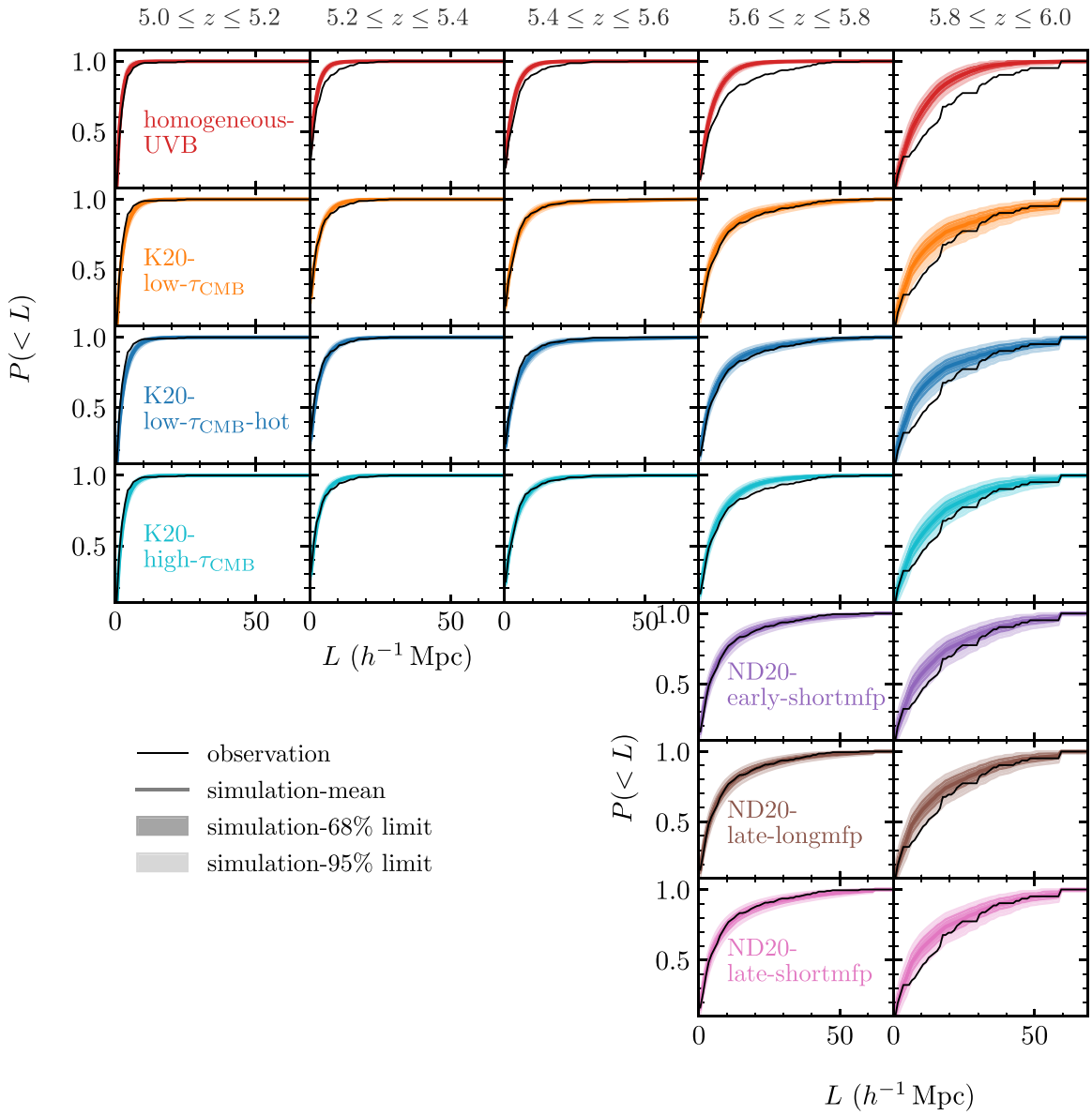

Figure 13. Cumulative distributions of dark gap length. In each redshift bin, the black line shows $P(< L)$ of the observed dark gaps. Dark gaps extending beyond the boundaries of the $\Delta z = 0.2$ window are truncated at the edge. The colored lines and dark/light-shaded regions represent the mean and 68%/95% limits, respectively, of $P(< L)$ in mock samples drawn from the models. In this figure, we use a high-mass-resolution run from the Sherwood Simulation Suite (Bolton et al. 2017) for the `homogeneous-UVB` model instead of the fiducial configuration. See text for details.

later and more rapid reionization histories. For example, the `K20-low-`$\tau_{\rm CMB}$ and `K20-low-`$\tau_{\rm CMB}$`-hot` models, which have a reionization midpoint of $z_{50} = 6.7$, is somewhat more consistent (see curves and shades near $5.6 \leqslant z \leqslant 5.8$ in Figures 12, 13, and 14) with the dark gap statistics at $z < 6$ than the `K20-high-`$\tau_{\rm CMB}$ mode, for which $z_{50} = 8.4$. A late and rapid reionization is also suggested by the recent mean free path measurement from Becker et al. (2021) (see also Cain et al. 2021; Davies et al. 2021).

Alternatively, long dark gaps can arise from a fully reionized IGM provided that there are large UVB fluctuations. The early reionization model from Nasir & D'Aloisio (2020), which retains postreionization fluctuations in the UV background and IGM temperature, is consistent with the data over at least $5.6 < z < 6.0$, where the available simulation outputs allow mock spectra to be compared to the data using the methods described above. Extending these simulations down to lower redshifts would be helpful for testing the pure fluctuating UVB model further.

6. Summary

In this paper, we present a search for dark gaps in the Lyα forest over $5 < z < 6$. We use high-S/N spectra of 55 QSOs at $z_{\rm em} > 5.5$ taken with Keck ESI and VLT X-Shooter, including data from the new XQR-30 VLT Large Programme. We focus on two statistics: the fraction of sightlines containing dark gaps of length $L \geqslant 30h^{-1}$ Mpc as a function of redshift, F_{30}, which we introduce here for the first time, and the dark gap length distribution, $P(< L)$. Our primary goal is to quantify the persistence of large Lyα-opaque regions in the IGM below redshift six, and to evaluate the consistency between the observed dark gap statistics and predictions from various models. We include a model with a fully ionized IGM and a uniform ionizing UV background, and others with large islands

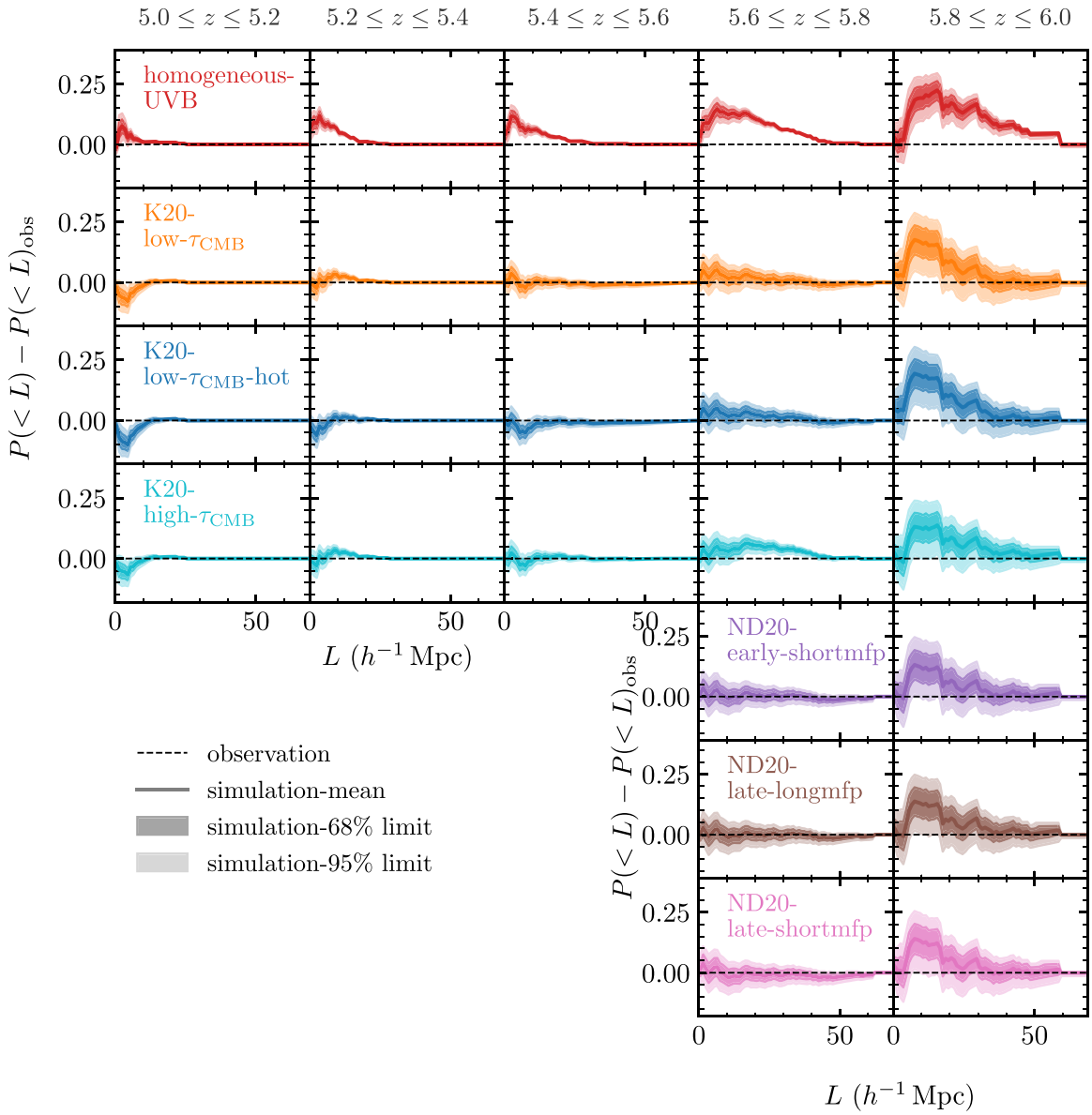

Figure 14. Similar to Figure 13, but showing the differences on cumulative distributions of dark gap length between the models and the observations.

of neutral gas and/or UVB fluctuations. Our main results can be summarized as follows:

1. We identify 50 long dark gaps ($L \geqslant 30h^{-1}$ Mpc) in the Lyα forest from our sample. Two long dark gaps are found at $z < 5.5$, with one extending down to $z \simeq 5.3$. We also report new ultralong dark gaps ($L > 80h^{-1}$ Mpc) below $z = 6$, similar to the one previously reported toward ULAS J0148+0600 by Becker et al. (2015). The presence of long dark gaps at these redshifts demonstrates that large regions of the IGM remain opaque to Lyα down to $z \simeq 5.3$.
2. In terms of both F_{30} and $P(<L)$, a fully ionized IGM with a homogeneous UVB is disfavored by the data down to $z \simeq 5.3$.
3. Models wherein reionization ends significantly below redshift six (Keating et al. 2020a; Nasir & D'Aloisio 2020) are broadly consistent with the data. Among these, the data favor models with a reionization midpoint near $z \sim 7$ and an end at $z \simeq 5.3$ or later. In these models, dark gaps arise from a combination of neutral patches in the IGM and regions of low ionizing UV background, which are often adjacent to one another.
4. We also find consistency with a model wherein reionization ends by $z = 6$ but the IGM retains large fluctuations in the UV background (Nasir & D'Aloisio 2020), at least over $5.6 < z < 6.0$.

Overall, the evolution of dark gaps observed at $z < 6$ suggests that signatures of reionization remain present in the IGM until at least $z \simeq 5.3$ in the form of neutral hydrogen islands and/or fluctuations in the ionizing UV background. We note that this work focuses on dark gaps in the Lyα forest. Given its lower optical depth, however, Lyβ may also be a useful tool. For example, islands of neutral gas may tend to produce more long Lyβ troughs than are created by fluctuations in the UV background (e.g., Nasir & D'Aloisio 2020). These and other statistics should provide further details on how the IGM evolves near the end of reionization.

We thank Elisa Boera and Fahad Nasir for their help and useful discussion. We also thank the anonymous reviewer for their careful reading of the paper and thoughtful comments.

Y.Z., G.D.B., and H.M.C. were supported by the National Science Foundation through grants AST-1615814 and AST-1751404. H.M.C. was also supported by the National Science Foundation Graduate Research Fellowship Program under grant No. DGE-1326120. S.E.I.B. acknowledges funding from the European Research Council (ERC) under the European Union's Horizon 2020 research and innovation program (grant agreement No. 740246 "Cosmic Gas"). L.C.K. was supported by the European Union's Horizon 2020 research and innovation program under the Marie Skłodowska-Curie grant agreement No. 885990. F.B. acknowledges support from the Australian Research Council through Discovery Projects (award DP190100252) and Chinese Academy of Sciences (CAS) through a China–Chile Joint Research Fund (CCJRF1809) administered by the CAS South America Center for Astronomy (CASSACA). A.-C.E. acknowledges support by NASA through the NASA Hubble Fellowship grant # HF2-51434 awarded by the Space Telescope Science Institute, which is operated by the Association of Universities for Research in Astronomy, Inc., for NASA, under contract NAS5-26555. X.F. and J.Y. acknowledge support from the NSF grants AST 15-15115 and AST 19-08284. M.G.H. acknowledges support from the UKRI STFC (grant Nos. ST/N000927/1 and ST/S000623/1). G.K.'s research is partly supported by the Max Planck Society via a partner group grant. A.P. acknowledges support from the ERC Advanced Grant INTERSTELLAR H2020/740120. Parts of this work was supported by the Australian Research Council Centre of Excellence for All Sky Astrophysics in 3 Dimensions (ASTRO 3D), through project # CE170100013. F.W. thanks the support provided by NASA through the NASA Hubble Fellowship grant #HST-HF2-51448.001-A awarded by the Space Telescope Science Institute, which is operated by the Association of Universities for Research in Astronomy, Incorporated, under NASA contract NAS5-26555.

Based on observations collected at the European Southern Observatory under ESO programmes 060.A-9024(A), 084.A-0360(A), 084.A-0390(A), 084.A-0550(A), 085.A-0299(A), 086.A-0162(A), 086.A-0574(A), 087.A-0607(A), 088.A-0897(A), 091.C-0934(B), 096.A-0095(A), 096.A-0418(A), 097.B-1070(A), 098.A-0111(A), 098.B-0537(A), 0100.A-0243(A), 0100.A-0625(A), 0101.B-0272(A), 0102.A-0154(A), 0102.A-0478(A), 1103.A-0817(A), and 1103.A-0817(B).

Some of the data presented herein were obtained at the W. M. Keck Observatory, which is operated as a scientific partnership among the California Institute of Technology, the University of California and the National Aeronautics and Space Administration. The Observatory was made possible by the generous financial support of the W. M. Keck Foundation. The authors wish to recognize and acknowledge the very significant cultural role and reverence that the summit of Maunakea has always had within the indigenous Hawaiian community. We are most fortunate to have the opportunity to conduct observations from this mountain. Finally, this research has made use of the Keck Observatory Archive (KOA), which is operated by the W.M. Keck Observatory and the NASA Exoplanet Science Institute (NExScI), under contract with the National Aeronautics and Space Administration.

This work was performed using the Cambridge Service for Data Driven Discovery (CSD3), part of which is operated by the University of Cambridge Research Computing on behalf of the STFC DiRAC HPC Facility (www.dirac.ac.uk). The DiRAC component of CSD3 was funded by BEIS capital funding via STFC capital grants ST/P002307/1 and ST/R002452/1 and STFC operations grant ST/R00689X/1. This work further used the DiRAC@Durham facility managed by the Institute for Computational Cosmology on behalf of the STFC DiRAC HPC Facility. The equipment was funded by BEIS capital funding via STFC capital grants ST/P002293/1 and ST/R002371/1, Durham University and STFC operations grant ST/R000832/1. DiRAC is part of the National e-Infrastructure.

Facilities: Keck:II (ESI), VLT:Kueyen (X-Shooter).

Software: `Astropy` (Astropy Collaboration et al. 2013, 2018), `Matplotlib` (Hunter 2007), `NumPy` (Harris et al. 2020), `SpectRes` (Carnall 2017).

Appendix A
Numerical Convergence

Here we test the convergence of our results for the `homogeneous-UVB` model with different box sizes and mass resolutions. We denote different simulation configurations as `X_Y`, where X is the box size in comoving Mpc h^{-1} and Y $= [(\text{number of dark matter} + \text{baryon particles})/2]^{1/3}$. The fiducial configuration used in Section 3 is `160_2048`.

To calculate F_{30} with smaller boxes, we first stitch the short skewers to form 160 Mpc/h skewers, and then create mock spectra following the method described in Section 4.4. In Figure A1, we compare F_{30} for mock data generated from different simulation configurations. We find little dependence on box size. F_{30} decreases slightly with increasing mass resolution, though the differences are within the expected 68% scatter for the present sample size. We compare $P(<L)$ with different configurations to the baseline configurations by calculating $P(<L) - P(<L)_{\rm baseline}$ in Figure A2. For a fixed mass resolution and varying box size, we compare simulations to our fiducial `160_2048` simulation. For a fixed box size but varying mass resolution, we compare simulations to the `40_512` configuration, which has the same mass resolution of `160_2048`. Similar to F_{30}, the variations in $P(<L)$ with box size are relatively minor. The impact of mass resolution is more significant, especially for smaller L.

Figures A1 and A2 suggest that mass resolution has a larger impact than box size on our statistics, in the sense that simulations with lower mass resolutions tend to produce more long gaps and fewer short gaps. This is because weak, narrow Lyα transmission peaks tend to be suppressed at lower resolution. This effect may need to be considered for larger samples. We emphasize that the `homogeneous-UVB` models that we are using for these convergence tests contain significantly fewer long gaps than the late reionization and fluctuating UVB models. It is therefore unclear how well the trends we see for large L would apply to these models, although it is likely that the effects of mass resolution we see at smaller gap lengths would generally be present in SPH simulations.

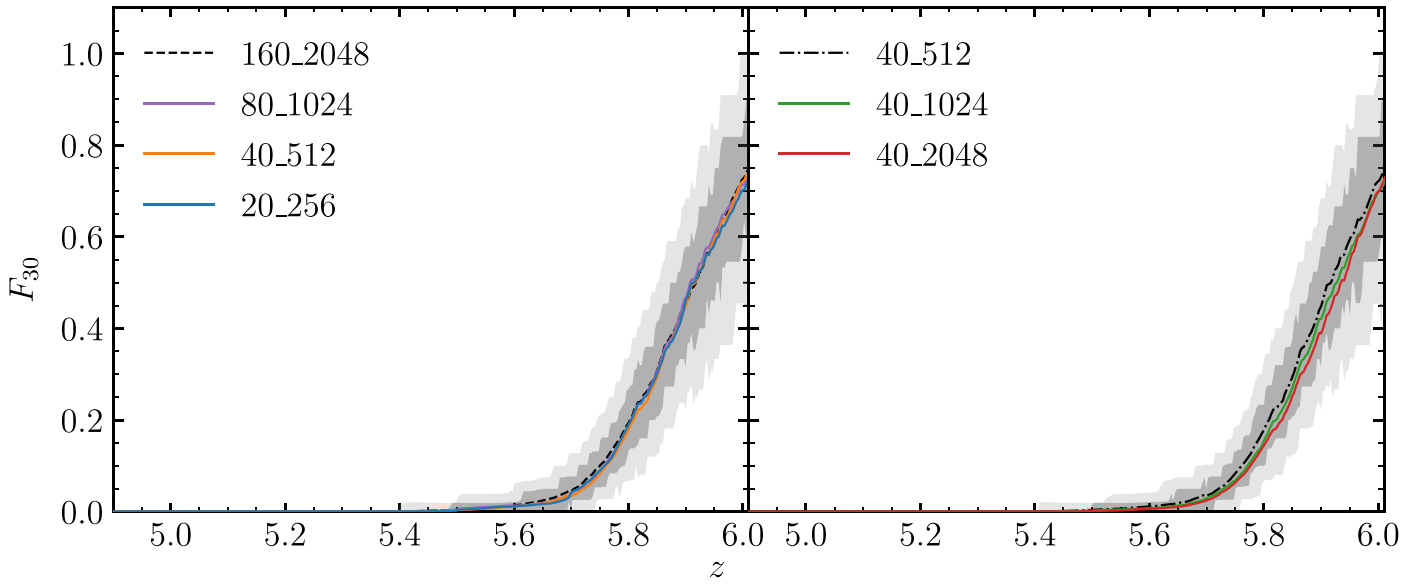

Figure A1. Fractions of QSO spectra exhibiting long ($L \geqslant 30h^{-1}$ Mpc) dark gaps as a function of redshift with different simulation configurations. The left panel compares results for varying box sizes but fixed mass resolution. The dark gray and light gray shaded regions are the 68% and 95% limits on the expected scatter for the present sample size from the `160_2048` simulation, which are the same as the shaded regions in Figure 12. The right panel compares results for varying mass resolutions but fixed box size. The dashed–dotted line is the mean, and shaded regions are 68% and 95% limits of the prediction from the `40_512` simulation.

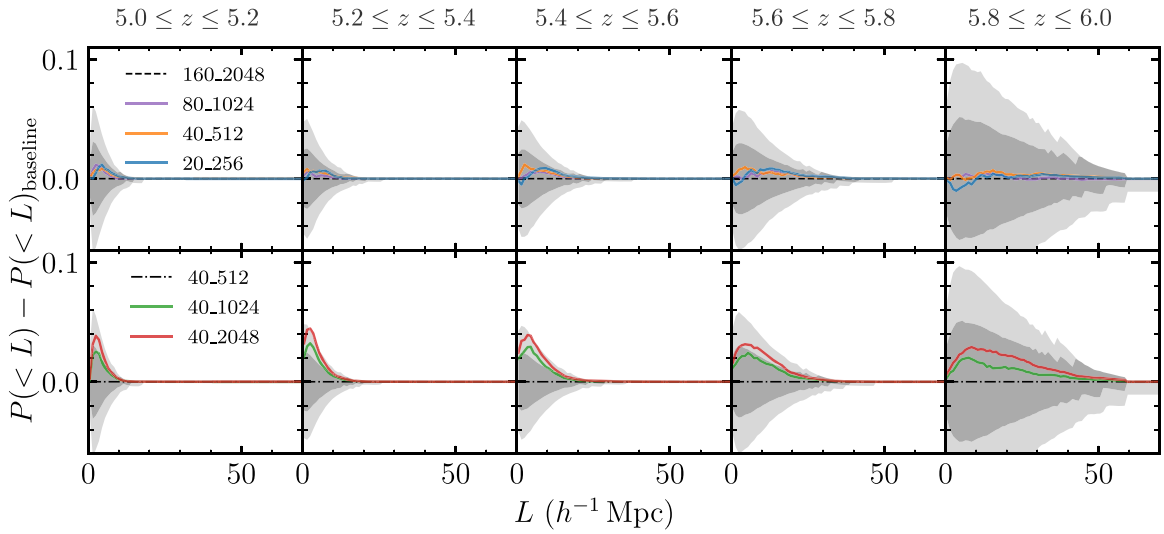

Figure A2. Difference on dark gap length distributions for different box sizes and mass resolutions compared to the baseline configurations. The top and bottom rows compare results for varying box sizes and varying mass resolutions, respectively. The dark gray and light gray shaded regions are the 68% and 95% limits on the expected scatter for the present sample size from the `160_2048` simulation (Top panel) and from the `40_512` simulation (Bottom panel).

Appendix B
Simulation Predictions without Masking

For consistency with the observations, we mask out small wavelength regions in the mock spectra that coincide with peaks in the observed flux error arrays, as described in Section 3.1. Figure B1 shows how the simulation results change without masking. The model predictions for F_{30} decrease because the masks sometimes fall on transmission peaks. The overall impact is minor; however, we emphasize that the observations should be compared to the simulation results with masking included.

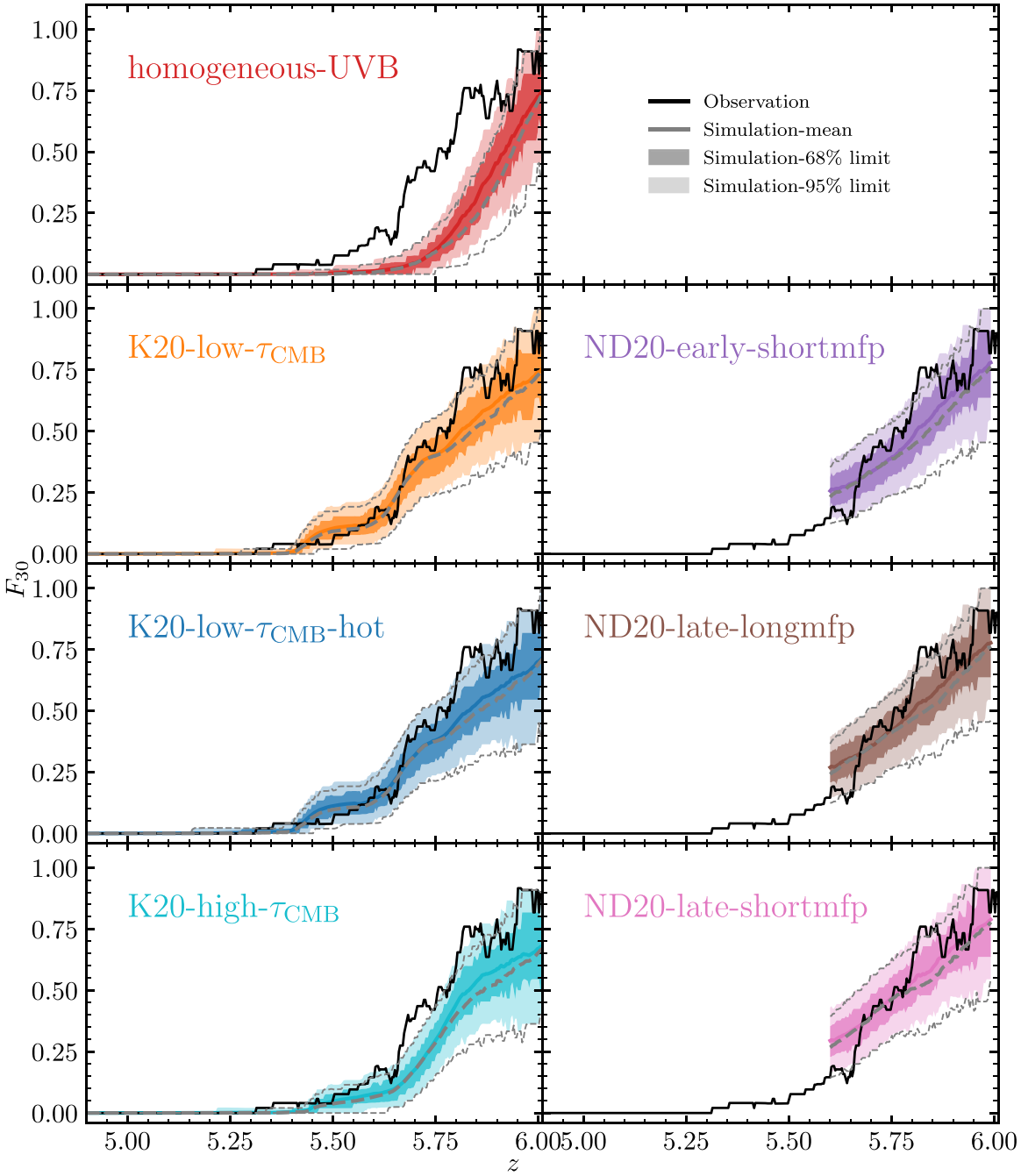

Figure B1. The fraction of sightlines located in dark gaps with $L \geqslant 30h^{-1}$ Mpc as a function of redshift. The dashed thick (thin) lines show the mean values (95% range) of simulation predictions without masking regions in the mock spectra that coincide with peaks in the flux error array. Other lines and shaded regions are as described in Figure 12.

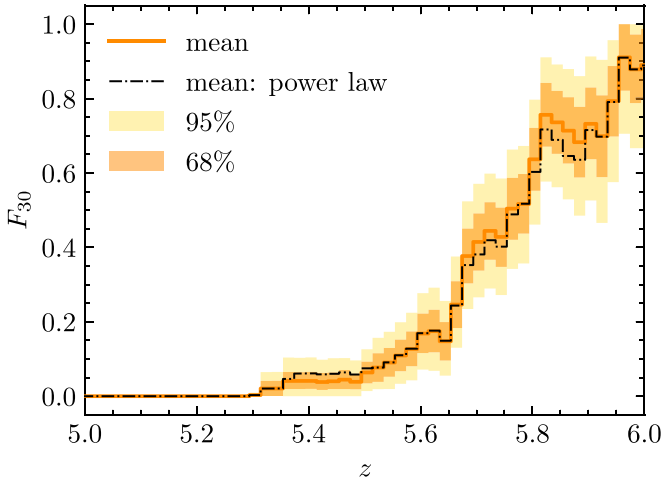

Figure C1. Measured fraction of QSO spectra exhibiting long ($L \geqslant 30h^{-1}$ Mpc) dark gaps as a function of redshift. The dotted–dashed line shows the result based on the power law continuum fitting. Other lines and regions are as described in Figure 5.

Appendix C
F_{30} Based on the Power-law Continuum Fitting

For reference, in this section, we calculate F_{30} based on the power-law continuum fitting. The power-law continua are in the form of $a\lambda^{-b}$, with a and b being free parameters. We generally estimate the power-law continua over ∼1285-1350 Å in the rest frame, which is relatively free of emission lines, and we extend the fitting range out to ∼2000 Å when possible. Figure C1 compares the results. The consistency (within 1σ) between F_{30} based on the PCA continuum and power law continuum suggests that our results are insensitive to continuum-fitting methods.

Appendix D
Effect of Metal Absorbers on F_{30}

The strong H I absorption typically associated with metal systems may potentially impact the observed F_{30} by connecting otherwise shorter gaps. We test whether this effect could be significant by dividing dark gaps at the redshifts of DLAs and other metal systems. We also exclude a 3000 km s^{-1} region surrounding the redshift of the metal absorber in order to allow for extended DLA absorption and/or strong absorbers clustered around the metal system. As shown in Figure D1, the impact on F_{30} is relativel minor, with a maximum decrease of ∼0.1 at $z \sim 5.8$. We caution that list of metal absorbers used here may be incomplete; however, we have verified that the three long dark gaps at $z \lesssim 5.5$ in particular do not contain metals to within the sensitivity of our data. In summary, we find that the impact of metal systems on F_{30} in this regard is minor, and that the `homogenous-UVB` model is strongly ruled out regardless of how these systems are treated.

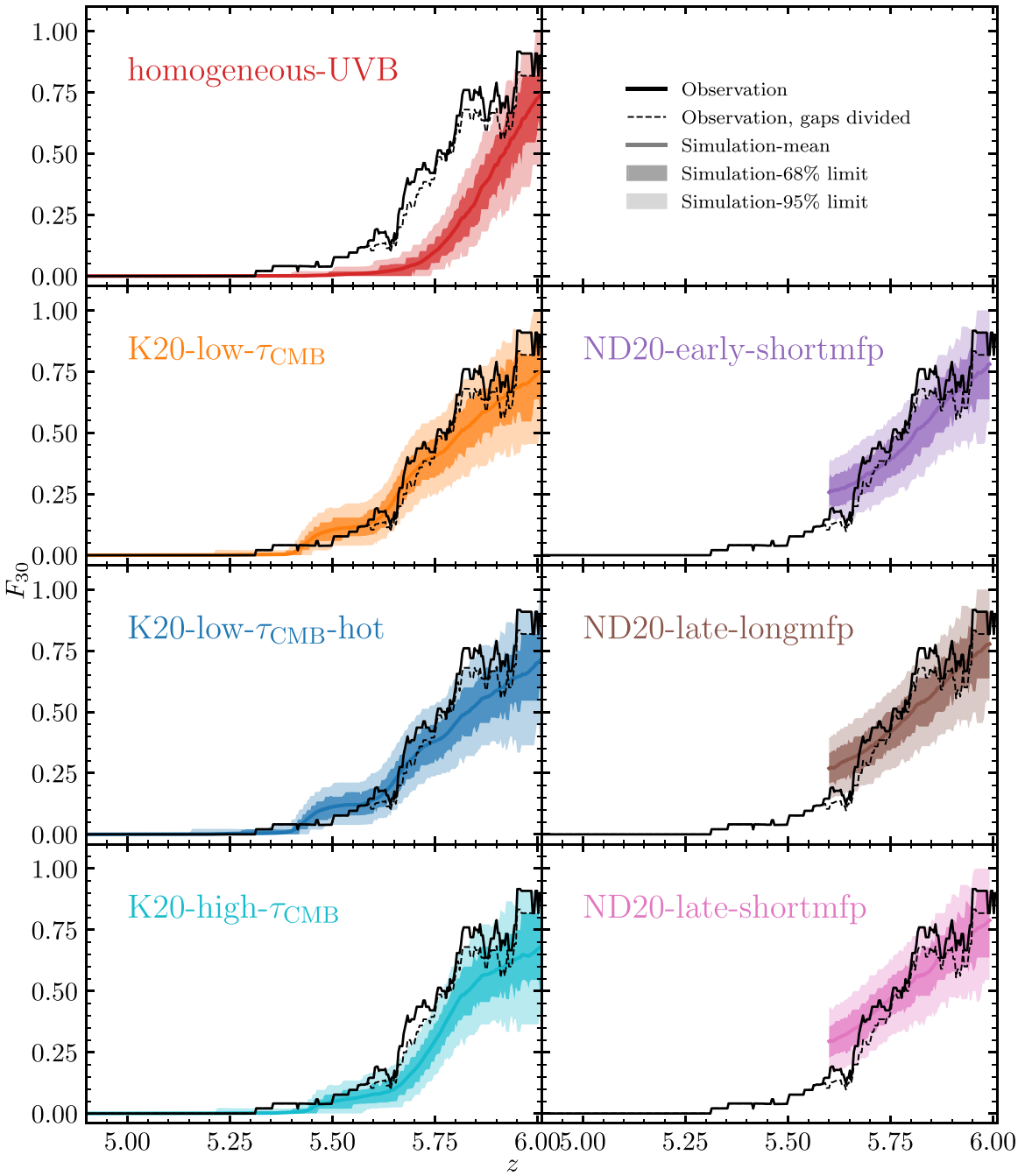

Figure D1. The fraction of sightlines located in dark gaps with $L \geqslant 30h^{-1}$ Mpc as a function of redshift. The dashed lines show F_{30} from observations with dark gaps divided at the redshifts of DLAs or metal systems with a 3000 km s^{-1} interval. Other lines and shaded regions are as described in Figure 12.

ORCID iDs

Yongda Zhu https://orcid.org/0000-0003-3307-7525
George D. Becker https://orcid.org/0000-0003-2344-263X
Sarah E. I. Bosman https://orcid.org/0000-0001-8582-7012
Laura C. Keating https://orcid.org/0000-0001-5211-1958
Holly M. Christenson https://orcid.org/0000-0002-0421-065X
Eduardo Bañados https://orcid.org/0000-0002-2931-7824
Fuyan Bian https://orcid.org/0000-0002-1620-0897
Frederick B. Davies https://orcid.org/0000-0003-0821-3644
Valentina D'Odorico https://orcid.org/0000-0003-3693-3091
Anna-Christina Eilers https://orcid.org/0000-0003-2895-6218
Xiaohui Fan https://orcid.org/0000-0003-3310-0131
Martin G. Haehnelt https://orcid.org/0000-0001-8443-2393
Girish Kulkarni https://orcid.org/0000-0001-5829-4716
Andrea Pallottini https://orcid.org/0000-0002-7129-5761
Yuxiang Qin https://orcid.org/0000-0002-4314-1810
Feige Wang https://orcid.org/0000-0002-7633-431X
Jinyi Yang https://orcid.org/0000-0001-5287-4242

References

Astropy Collaboration, Price-Whelan, A. M., Sipőcz, B. M., et al. 2018, AJ, 156, 123
Astropy Collaboration, Robitaille, T. P., Tollerud, E. J., et al. 2013, A&A, 558, A33

Aubert, D., & Teyssier, R. 2008, MNRAS, 387, 295
Aubert, D., & Teyssier, R. 2010, ApJ, 724, 244
Bañados, E., Decarli, R., Walter, F., et al. 2015, ApJL, 805, L8
Bañados, E., Venemans, B. P., Mazzucchelli, C., et al. 2018, Natur, 553, 473
Barnett, R., Warren, S. J., Becker, G. D., et al. 2017, A&A, 601, A16
Becker, G. D., Bolton, J. S., Madau, P., et al. 2015, MNRAS, 447, 3402
Becker, G. D., D'Aloisio, A., Christenson, H. M., et al. 2021, MNRAS, 508, 1853
Becker, G. D., Davies, F. B., Furlanetto, S. R., et al. 2018, ApJ, 863, 92
Becker, G. D., Pettini, M., Rafelski, M., et al. 2019, ApJ, 883, 163
Boera, E., Becker, G. D., Bolton, J. S., & Nasir, F. 2019, ApJ, 872, 101
Bolton, J. S., Puchwein, E., Sijacki, D., et al. 2017, MNRAS, 464, 897
Bosman, S. E. I., Davies, F. B., Becker, G. D., et al. 2021a, arXiv:2108.03699
Bosman, S. E. I., Ďurovčíková, D., Davies, F. B., & Eilers, A. C. 2021b, MNRAS, 503, 2077
Bosman, S. E. I., Fan, X., Jiang, L., et al. 2018, MNRAS, 479, 1055
Bromm, V., & Larson, R. B. 2004, ARA&A, 42, 79
Cain, C., D'Aloisio, A., Gangolli, N., & Becker, G. D. 2021, ApJL, 917, L37
Carilli, C. L., Neri, R., Wang, R., et al. 2007, ApJ, 666, L9
Carnall, A. C. 2017, arXiv:1705.05165
Chardin, J., Puchwein, E., & Haehnelt, M. G. 2017, MNRAS, 465, 3429
Chen, S.-F. S., Simcoe, R. A., Torrey, P., et al. 2017, ApJ, 850, 188
Choudhury, T. R., Paranjape, A., & Bosman, S. E. I. 2021, MNRAS, 501, 5782
Christenson, H. M., Becker, G. D., Furlanetto, S. R., et al. 2021, ApJ, 923, 87
D'Aloisio, A., McQuinn, M., & Trac, H. 2015, ApJL, 813, L38
Davies, F. B., Bosman, S. E. I., Furlanetto, S. R., Becker, G. D., & D'Aloisio, A. 2021, ApJL, 918, L35
Davies, F. B., & Furlanetto, S. R. 2016, MNRAS, 460, 1328
Davies, F. B., Hennawi, J. F., Bañados, E., et al. 2018a, ApJ, 864, 142
Davies, F. B., Hennawi, J. F., Bañados, E., et al. 2018b, ApJ, 864, 143
Dayal, P., & Ferrara, A. 2018, PhR, 780, 1
de Belsunce, R., Gratton, S., Coulton, W., & Efstathiou, G. 2021, MNRAS, 507, 1072
Decarli, R., Walter, F., Venemans, B. P., et al. 2018, ApJ, 854, 97
Eilers, A.-C., Davies, F. B., & Hennawi, J. F. 2018, ApJ, 864, 53
Eilers, A.-C., Davies, F. B., Hennawi, J. F., et al. 2017, ApJ, 840, 24
Eilers, A.-C., Hennawi, J. F., Decarli, R., et al. 2020, ApJ, 900, 37
Fan, X., Strauss, M. A., Becker, R. H., et al. 2006, AJ, 132, 117
Furlanetto, S. R., Hernquist, L., & Zaldarriaga, M. 2004, MNRAS, 354, 695
Gaikwad, P., Srianand, R., Haehnelt, M. G., & Choudhury, T. R. 2021, MNRAS, 506, 4389
Gallerani, S., Ferrara, A., Fan, X., & Choudhury, T. R. 2008, MNRAS, 386, 359
Gnedin, N. Y., Becker, G. D., & Fan, X. 2017, ApJ, 841, 26
Greig, B., Mesinger, A., & Bañados, E. 2019, MNRAS, 484, 5094
Greig, B., Mesinger, A., Haiman, Z., & Simcoe, R. A. 2017, MNRAS, 466, 4239
Haardt, F., & Madau, P. 2012, ApJ, 746, 125
Harris, C. R., Millman, K. J., van der Walt, S. J., et al. 2020, Natur, 585, 357
Hoag, A., Bradač, M., Huang, K., et al. 2019, ApJ, 878, 12
Horne, K. 1986, PASP, 98, 609
Hu, W., Wang, J., Zheng, Z.-Y., et al. 2019, ApJ, 886, 90
Hunter, J. D. 2007, CSE, 9, 90
Jiang, L., Fan, X., Vestergaard, M., et al. 2007, AJ, 134, 1150
Jones, A., Noll, S., Kausch, W., Szyszka, C., & Kimeswenger, S. 2013, A&A, 560, A91
Jung, I., Finkelstein, S. L., Dickinson, M., et al. 2020, ApJ, 904, 144
Kashino, D., Lilly, S. J., Shibuya, T., Ouchi, M., & Kashikawa, N. 2020, ApJ, 888, 6
Keating, L. C., Kulkarni, G., Haehnelt, M. G., Chardin, J., & Aubert, D. 2020a, MNRAS, 497, 906
Keating, L. C., Weinberger, L. H., Kulkarni, G., et al. 2020b, MNRAS, 491, 1736
Kelson, D. D. 2003, PASP, 115, 688
Kulkarni, G., Keating, L. C., Haehnelt, M. G., et al. 2019a, MNRAS, 485, L24
Kulkarni, G., Worseck, G., & Hennawi, J. F. 2019b, MNRAS, 488, 1035
Kurk, J. D., Walter, F., Fan, X., et al. 2007, ApJ, 669, 32
Maiolino, R., Cox, P., Caselli, P., et al. 2005, A&A, 440, L51
Mason, C. A., Fontana, A., Treu, T., et al. 2019, MNRAS, 485, 3947
Mason, C. A., Treu, T., Dijkstra, M., et al. 2018, ApJ, 856, 2
Mazzucchelli, C., Bañados, E., Venemans, B. P., et al. 2017, ApJ, 849, 91
McGreer, I. D., Mesinger, A., & D'Odorico, V. 2015, MNRAS, 447, 499
McQuinn, M. 2016, ARA&A, 54, 313
Meiksin, A. 2020, MNRAS, 491, 4884
Nasir, F., & D'Aloisio, A. 2020, MNRAS, 494, 3080
Noll, S., Kausch, W., Barden, M., et al. 2012, A&A, 543, A92
Parsa, S., Dunlop, J. S., & McLure, R. J. 2018, MNRAS, 474, 2904
Paschos, P., & Norman, M. L. 2005, ApJ, 631, 59
Planck Collaboration, Aghanim, N., Akrami, Y., et al. 2020, A&A, 641, A6
Qin, Y., Mesinger, A., Bosman, S. E. I., & Viel, M. 2021, MNRAS, 506, 2390
Sheinis, A. I., Bolte, M., Epps, H. W., et al. 2002, PASP, 114, 851
Shen, Y., Wu, J., Jiang, L., et al. 2019, ApJ, 873, 35
Songaila, A., & Cowie, L. L. 2002, AJ, 123, 2183
Springel, V. 2005, MNRAS, 364, 1105
Trac, H., & Pen, U.-L. 2004, NewA, 9, 443
Venemans, B. P., Walter, F., Neeleman, M., et al. 2020, ApJ, 904, 130
Vernet, J., Dekker, H., D'Odorico, S., et al. 2011, A&A, 536, A105
Walther, M., Oñorbe, J., Hennawi, J. F., & Lukić, Z. 2019, ApJ, 872, 13
Wang, F., Davies, F. B., Yang, J., et al. 2020, ApJ, 896, 23
Wang, F., Fan, X., Yang, J., et al. 2021, ApJ, 908, 53
Wang, F., Wang, R., Fan, X., et al. 2019, ApJ, 880, 2
Wang, R., Carilli, C. L., Neri, R., et al. 2010, ApJ, 714, 699
Wang, R., Wagg, J., Carilli, C. L., et al. 2013, ApJ, 773, 44
Wold, I. G. B., Malhotra, S., Rhoads, J., et al. 2021, arXiv:2105.12191
Yang, J., Venemans, B., Wang, F., et al. 2019, ApJ, 880, 153
Yang, J., Wang, F., Fan, X., et al. 2020a, ApJ, 897, L14
Yang, J., Wang, F., Fan, X., et al. 2020b, ApJ, 904, 26